

# Nonlinear aging of cylindrical lithium-ion cells linked to heterogeneous compression



Tobias C. Bach<sup>a,\*</sup>, Simon F. Schuster<sup>b</sup>, Elena Fleder<sup>a</sup>, Jana Müller<sup>a</sup>, Martin J. Brand<sup>b</sup>, Henning Lormann<sup>a</sup>, Andreas Jossen<sup>b</sup>, Gerhard Sextl<sup>a</sup>

<sup>a</sup> Fraunhofer Institute for Silicate Research, Neunerplatz 2, 97082 Würzburg, Germany

<sup>b</sup> Institute for Electrical Energy Storage Technology, Technische Universität München, Arcisstraße 21, 80333 Munich, Germany

## ARTICLE INFO

### Article history:

Received 12 October 2015

Received in revised form 12 January 2016

Accepted 12 January 2016

Available online 24 January 2016

### Keywords:

Aging  
Plating  
Graphite  
Compression  
Cycle life  
Post mortem

## ABSTRACT

Second-life applications of automotive lithium-ion batteries are currently investigated for grid stabilization. Reutilization depends on reliable projections of the remaining useful life. However, reports on sudden degradation of lithium-ion-cells near 80% state of health challenge these extrapolations. Sudden degradation was demonstrated for different positive active materials. This work elucidates the cause of sudden degradation in detail. As part of a larger study on nonlinear degradation, in-depth analyses of cells with different residual capacities are performed. Sudden degradation of capacity is found to be triggered by the appearance of lithium plating confined to small characteristic areas, generated by heterogeneous compression. The resulting lithium loss rapidly alters the balancing of the electrodes, thus generating a self-amplifying circle of active material and lithium loss. Changes in impedance and open-circuit voltage are explained by the expansion of degraded patches. Destructive analysis reveals that sudden degradation is caused by the graphite electrode while the positive electrode is found unchanged except for delithiation caused by side reactions on the negative electrode. Our findings illustrate the importance of homogeneous compression of the electrode assembly and carbon electrode formulation. Finally, a quick test to evaluate the vulnerability of cell designs toward sudden degradation is proposed.

© 2016 The Authors. Published by Elsevier Ltd. This is an open access article under the CC BY license (<http://creativecommons.org/licenses/by/4.0/>).

## 1. Introduction

Lithium-ion batteries are the most advanced technology for energy storage devices due to their high energy density and efficiency [1,2]. In various fields such as consumer devices or electrified vehicles, lithium-ion technology enables new applications. The current uncertainty regarding the reachable use time inhibits deeper market penetration. Reports in literature about suddenly increasing aging rates raise concern regarding the viability of aging models and their use in lifetime projections [3–5]. In this work, the aging effect is investigated in detail. Probable root causes are presented. Furthermore, design imperfections and use conditions leading to such unfavorable behavior are discussed as well.

Lithium-ion battery aging is a complex process with several influencing degradation mechanisms as shown by recent studies on commercial batteries [3,4,6–11]. For conciseness, only the main

influence factors are discussed here since recent reviews [12–14] already provide a broad view on aging processes. In aging models, the capacity fade is mainly attributed to the formation of passive films, leading to lithium loss and resistance increase, as both negative and positive electrodes are usually operated outside the electrolyte's electrochemical stability window [12]. Lithium loss is generally attributed to the solid electrolyte interphase (SEI) on the negative electrode, while passive films on the positive electrode are associated to rising resistance. Studies on electrolyte aging have shown the impact of carbonate and LiPF<sub>6</sub> decomposition [15–19] as well as the mitigating effects of additives [20,21]. The calendric capacity fade resulting from passive film formation has been shown to have a square root dependency on time [4,10,13,22,23]. Nearly linear aging behavior has been reported to be influenced by additional aging factors [3]. It is usually reported that cyclic aging causes linear fading of capacity and square root dependencies on charge throughput are sometimes reported as well [3,13,24,25]. SEI formation, causing lithium loss and increasing resistance, is reported to be the dominant source of capacity fade. The linear aging model may be used for projections of SEI growth and residual value of aged cells and battery packs, but

\* Corresponding author. Fax: +49 9314100570.

E-mail addresses: [tobias.bach@isc.fraunhofer.de](mailto:tobias.bach@isc.fraunhofer.de), [tcbach@live.com](mailto:tcbach@live.com) (T.C. Bach).

reports on suddenly increasing aging rates put such projections into question [3,4,26]. The inflection point has been linked to partially irreversible lithium plating [4]. The occurrence of inactive lithium, which is not stripped upon full discharge of the cell, is noteworthy as it shows the possibility of irreversible capacity loss due to local disconnection of parts of the electrodes' electrochemically active materials. While counterintuitive, incomplete stripping of lithium metal is a well-described effect of the solid electrolyte interphase [27–30] and has been shown to lead to effective loss of lithium on model substrates [31,32] and on graphite electrodes in cycled batteries [14,33–36]. Also in this study, we found inactive lithium on the nearly totally delithiated graphite electrode despite the potential difference of more than 0.5 V. As inactive lithium is not in electrical contact to the electrode, it is difficult to detect by electric means, while it is easily detected by post-mortem observation.

In a recent article [37] the regimes leading to sudden degradation in lithium-ion batteries are investigated on cell level. Control regimes causing sudden degradation are identified and guidelines for avoidance are given. The identified factors leading to the sudden degradation of usable capacity are high depth of discharge, high charging currents and low temperatures. Cells cycled between 3.0 V and 4.2 V with constant current charging at 0.5 C and constant current discharging with 1 C exhibited normal behavior up to 800 equivalent full cycles as shown in Fig. 1. Based on the observed behavior it appears reasonable to predict several hundred additional cycles above 60% residual capacity. However, a sudden increase in degradation rate occurs at about 80% residual capacity. Only 150 cycles later the cell has lost more than half of its initial capacity.

In this work, we investigate cells exposed to this cyclic aging protocol at three different stages of aging. Expanding upon previous work, we deliver an insight into the chemical changes inside the cells from which the behavior was described before [37]. Uncycled, pristine cells (A) are compared to cycled cells that have just started to increase their aging rate (B) and cells that have already degraded significantly (C). Causes and effects are investigated in detail. Using destructive analysis, so called post-mortem studies, cells are characterized on the component level by electrochemical methods and chemical analyses. The influence of cell design on aging is discussed. Furthermore, possible mechanisms of sudden rapid aging are explained on component level. Moreover, the reasons for sudden degradation, as well as design and control countermeasures are explained. Finally, a quick test for the vulnerability of cell designs toward nonlinear degradation is proposed.

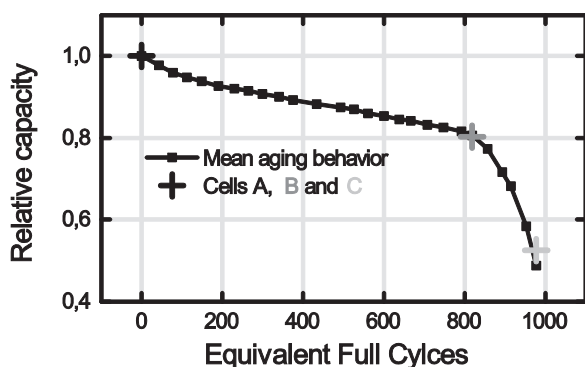


**Fig. 1.** The cells show a strong increase in aging at about 80% residual capacity. Cells are further analyzed in uncycled state (A), as they just start to age faster (B) and after the kink in capacity (C).

## 2. Experimental

In this study, lithium-ion cells with lithium–nickel–manganese–Cobalt oxide (NMC) based positive and graphite based negative electrodes were investigated. The cylindrical Molicel IHR18650A by E-One Moli Energy Corp. has a nominal capacity of 1.95 Ah. Cells called pristine in this article have undergone formation procedures at the discretion of the manufacturer. The utilized instruments are listed in Table 1.

Cells A–C were obtained from a large aging experiment [37]. In this study they were cycled with constant current between 3.0 V and 4.2 V. Charging was carried out at 0.5 C and discharging at 1 C.

For a quick test to evaluate the vulnerability toward plating and for thermography a constant current, constant voltage scheme was used for both charge and discharge procedures to exert maximal stress. For control experiments in Sections 3.3 and 3.4, the charging current was chosen to be 1 C, while the discharge current was set to 2 C. Constant Voltage steps at 3.0 V and 4.2 V were maintained until the current dropped below 0.1 C for more than one second. Ambient temperature was held at 20 °C.

Prior to destructive analysis, cells were characterized with a 0.02 C full cycle between 3.0 V and 4.2 V, as well as a checkup procedure as described in our previous work [37]. The 18650 cells were discharged to 3.0 V with a constant voltage step held until the current dropped below 0.1 C. Then, the cells were opened in a glovebox with controlled argon atmosphere.

Preparation for electrochemical analysis and scanning electron microscopy (SEM) was entirely carried out under argon and samples for SEM were transferred under vacuum without washing steps or contact to air using a custom sample holder. Samples for inductively coupled plasma optical emission spectroscopy (ICP-OES) and X-ray diffraction (XRD) were handled in air.

Samples for ICP-OES from both negative and positive electrodes were taken, washed and dried under argon atmosphere. Washing was performed by soaking samples in dimethyl carbonate (MERCK SelectyLite™) for 60 min, renewing the dimethyl carbonate solution and soaking for another 30 min. The samples were then dried under vacuum using the antechamber of the glovebox and weighted under argon atmosphere. Samples were then exposed to air and dissolved using *aqua regia*. *Aqua regia*, a strong oxidizing acid, was obtained by freshly mixing three volume parts of concentrated hydrochloric acid (fuming 37%, for analysis, MERCK) with one volume part of concentrated nitric acid (concentrated 65%, p.a., Th. Geyer). The samples were stirred in *aqua regia* overnight. All metal parts and active materials were oxidized and dissolved so that only graphite and binder remained as solid residue. The solid residue was filtered off and weighted. The obtained clear solutions containing the metal species were then analyzed by ICP-OES. ICP-OES-measurements were run using a glass cyclonic-action spraychamber with glass concentric nebulizer for the sample introduction and a radially viewed plasma. The interpretation of signals was performed using repeat measurements of samples and calibration standards prepared in 1% hydrochloric acid. The wavelengths used for the analysis of element concentrations are shown in Table 2. The output was averaged over all monitored wavelengths.

Using a custom-built computer tomograph based on a 225 kV X-ray tube, flat panel detector and rotary sample stage, complete volume information of pristine cells of the same type was reconstructed. XRD of positive electrode samples was performed under air.

Temperature gradients were investigated by thermal imaging. As the battery was covered by polymer based shrink wrap, its emissivity was estimated to be 0.95. Thermal images and temperature values from three points on the surface were collected while the battery was cycled.

**Table 1**

Instruments used in this work. The most relevant parameters are given.

Method	Instrument	Operating parameters
SEM	Zeiss Supra 25	Acceleration voltage 3–15 kV; secondary electron detector
ICP-OES	Varian Vista-PRO	<2% uncertainty for main elements; <5% uncertainty for elements with an absolute concentration <0.2%
XRD	PANalytical Empyrean	Copper K-alpha line, recorded from 10 to 70° in 2θ with an increment of 0.02°
Thermal imaging	FLIR T650	Uncooled Microbolometer; noise equivalent differential temperature at 30 °C < 0.02 °C; accuracy ± 1 °C or 1% of absolute value
Galvanostatic cycling	Maccor Series 4000	Voltage 0–5 V, current 0–5 A; accuracy 0.02% of full scale

**Table 2**

Wavelengths used for ICP-OES Analysis.

Element	Wavelength monitored/nm
Lithium	610.4
Manganese	257.6, 259.4, 260.6, 294.9
Nickel	216.6, 221.6, 230.3, 231.6
Cobalt	228.6, 230.8, 237.9, 238.9

For locally resolved electrochemical characterization, small test cells with reference electrodes were constructed from different parts of the jelly roll. Using a hollow punch, samples of 18 mm diameter were taken from the locations shown in Fig. 2 from negative and positive electrodes, respectively. By combining cell identification and sample location, we provide an unambiguous nomenclature. Samples are named by the letter (A–C) of the respective cell and the number of the sampling location (1–6). The active material coating was scratched off on one side of the electrode discs to contact the current collector. The coordinate system in Fig. 2 shows the naming conventions used for directions. Based on the cylindrical form of the cell, the direction of the mandrel, around which the electrode is wound, is called axial. The vector pointing through the electrode layers is called radial and the vector parallel to the long side of the electrode is called angular.

The electrode discs obtained were used to construct laboratory cells with a glass fiber separator, standard electrolyte and a lithium reference. Commercial three-electrode laboratory cells (El-Cell Ref) were used. A 1.5 mm thick glass fiber separator was necessary for the placement of a reference electrode. In contrast, the separator in the original cell has a thickness of only 25 μm. As the separator was one order of magnitude thicker than the one in the commercial battery, diffusion overpotentials differed. The systematic error induced by the separator was limited by applying low current densities only. A standard electrolyte, containing 1 mol l<sup>-1</sup> LiPF<sub>6</sub> in 1:1 EC:EMC (Selectipur LP50, MERCK) was used for laboratory cells. The same 0.02 C full cycle between 3.0 V and 4.2 V as used for the original cells was applied to the test cells. Using an auxiliary voltmeter, the voltage of the negative electrode with respect to the lithium metal reference electrode was

monitored. By controlling test cells in the same way as original ones and keeping current densities low, the results from the test cells could be used to understand the processes in the original cell.

Charge and discharge behavior of the overall cell and individual electrodes are represented using incremental capacity analysis, a method providing figures very similar to cyclic voltammetry. Incremental capacity was calculated using the differential quotient of the charge  $Q$  and the voltage  $V$  with respect to the time  $t$ : Incremental capacity =  $dQ/dV = [Q(t_2) - Q(t_1)]/[V(t_2) - V(t_1)]^{-1}$  with  $V(t_2) - V(t_1) \geq dV_{\min}$

When  $dV$  is calculated directly from the timeseries, small voltage increments combined with measurement noise may lead to amplified noise [38,39]. Therefore a minimum potential increment of  $dV_{\min} = 5$  mV was set for cathode and anode incremental capacity analyses. Accordingly, the full cell minimum increment was set to  $dV_{\min} = 10$  mV to obtain a comparable number of increments. The minimal increments were ensured for each step by increasing the time step until the condition was met.

### 3. Results and discussion

#### 3.1. Materials characterization

##### 3.1.1. Unaged cells

The negative active material is found to consist of non-spherical graphite particles with sizes in the order of 10 μm. The initial composition of the positive active material before formation is estimated to be  $\text{Li}_{1.11 \pm 0.02} \text{Ni}_{0.33 \pm 0.01} \text{Mn}_{0.33 \pm 0.01} \text{Co}_{0.33 \pm 0.01} \text{O}_2$  by summing up total lithium, nickel, manganese and cobalt contents of the positive and negative electrode of the pristine cell as measured using ICP-OES. The composition of the positive active material in the pristine cell is found to be  $\text{Li}_{1.06 \pm 0.02} \text{Ni}_{0.33 \pm 0.01} \text{Mn}_{0.33 \pm 0.01} \text{Co}_{0.33 \pm 0.01} \text{O}_2$ . The errors are derived from measurement uncertainty; oxygen content is inferred from crystal structure. The positive electrode, and therefore the cell, has a capacity of 3.0 mAh cm<sup>-2</sup>. 4.5% of total lithium content is found in the negative electrode of the discharged pristine cell. This initial lithium content can be attributed to the SEI formed during

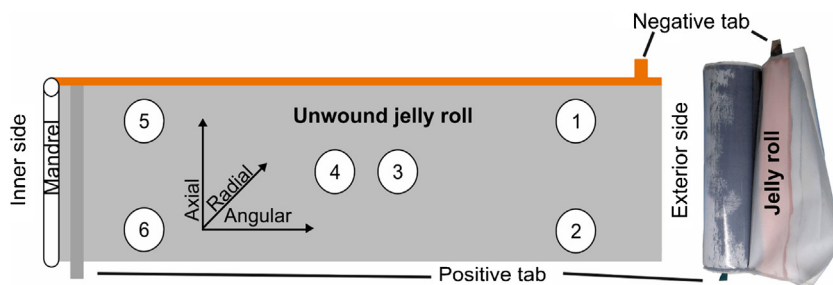


**Fig. 2.** Schematic showing the sample positions for spatially resolved electrochemical analysis on the unwound jelly roll. A partially unwound real jelly roll is shown for orientation. Schematic is not to scale.

formation and to intercalated lithium that remains in the negative electrode after formation.

### 3.1.2. Positive electrode

Visual inspection of the positive electrode does not reveal any changes except delamination effects upon unwinding of the jelly rolls. SEM micrographs confirm the absence of major changes in NMC morphology as already discussed in a previous publication [37]. The typical hierarchical structure, consisting of spherical particles several micrometers in diameter with a substructure showing a feature size below one micrometer appears unchanged even at pronounced aging states of the battery.

The XRD patterns in Fig. 3 show the good stability of the NMC host lattice that is also known from previous studies [31,41–43]. Based on XRD patterns of pristine NMC published by Choi et al. [40], peak positions and relative heights for NMC in different states of lithiation have been compared to the aged samples. The two lithiation states closest to those found in this study are used for comparison. Literature spectra of fully lithiated NMC ( $\text{LiNi}_{0.33}\text{Mn}_{0.33}\text{Co}_{0.33}\text{O}_2$ ) and partially delithiated NMC ( $\text{Li}_{0.7}\text{Ni}_{0.33}\text{Mn}_{0.33}\text{Co}_{0.33}\text{O}_2$ ) compare well to samples A–C. The crystal structure of all samples is intact and all peaks can be attributed to their respective miller indices. Rietveld refinement based on a reference pattern [44] yielded the lattice parameters given in Table 3.

Lattice parameters reported from pristine cells show an approximately linear dependency on lithiation [7,40,45,46]. Therefore, the change of lattice parameters can be used to determine the lithiation of NMC as shown in Fig. 4 and, combined with the initial lithium content  $c_0$  of  $5.59 \text{ mAh cm}^{-2}$ , the loss of lithium:

$$\text{Li-loss} = \Delta(\text{Lattice Parameter}) \text{ Slope}^{-1} c_0$$

The results shown in Table 3 point to considerable lithium loss. In contrast, degradation was not detected. Thus, morphology and crystallographic structure are found to be unchanged by SEM and XRD. Loss of lithium is the only change found at the NMC electrode. A thin passive layer inducing increased resistance might have formed, but is not detectable by the utilized methods.

### 3.1.3. Negative electrode

Fig. 5(a) shows photographs of the graphite electrodes of cells A–C. The graphite electrode of cell A appears totally black, as is expected from a functional discharged carbon based active material. A small area exhibiting lithium plating is found on the graphite electrode of cell B. Much larger areas of cell C are covered by metallic lithium and other residue. The finding of inactive

lithium confirms the previous work by Broussely et al., who also linked the finding of inactive lithium to the appearance of sudden degradation [4]. The photograph of the negative electrode extracted from Cell B shows well defined plating patterns. A thin stripe in angular direction, an area in the middle of the electrode and a regular pattern of axial stripes are much brighter than the surrounding graphite. The central area and the stripe pattern exhibit a metallic sheen Table 4

Chemical analyses by ICP-OES are utilized to investigate the passive layers found on the aged and pristine samples. Increased values of manganese, nickel, cobalt and lithium are found on the negative electrode of cell B. The negative electrode of cell C exhibits even higher levels. The loadings of washed out metals increase with aging. As manganese is associated with increased SEI formation [41,49] and as nickel and cobalt show similar behavior, only manganese and lithium contents are discussed here. A baseline manganese content of  $11 \text{ nmol cm}^{-2}$  is found in Cell A. In cell B, the manganese loading of the graphite electrode has risen to  $33 \text{ nmol cm}^{-2}$ . Due to the small size of the regions covered by plated lithium, they have not been sampled separately. On the other hand, in Cell C, the areas covered by plating were sufficiently large to be sampled and analyzed separately from the areas appearing unchanged. The loading found in areas appearing black has risen to  $46 \text{ nmol cm}^{-2}$ , approximately four times more than in the pristine sample. The sample taken from a region covered by a plated lithium moss is found to contain  $139 \text{ nmol cm}^{-2}$ , about twelve times more than in the baseline value and about three times than the quantity found in other areas of the same cell. The findings on inactive lithium follow the same trend. In order to illustrate the electrochemical impact, the findings are converted from  $\text{nmol cm}^{-2}$  to  $\text{mAh cm}^{-2}$ . In the pristine cell A, only  $0.25 \text{ mAh cm}^{-2}$  of inactive lithium are found on the graphite electrode. Furthermore, in cell B the amount of inactive lithium has more than doubled to  $0.55 \text{ mAh cm}^{-2}$ . In cell C  $0.85 \text{ mAh cm}^{-2}$  of inactive lithium are found on dark parts of the negative electrode. In an area with a visible surface film and a metallic sheen,  $1.87 \text{ mAh cm}^{-2}$  are found. The increase in inactive lithium amounts to about half of the initial active lithium content of the positive active material. The dramatic loss of lithium in degraded areas causes an important part of the overall loss of lithium inventory.

SEM observations confirm that areas appearing black are only slightly changed, while areas with visible plating are covered by a thick layer of degradation products. The degradation of the graphite electrode is shown in Fig. 5(b). The graphite particles of the negative electrode of cell A appear pristine. The black areas of cells B and C are covered by a thin passive layer only. Bright areas with visible plating are shown on the right. The surface film completely covers all graphite features in plated areas. SEM-EDX analyses show that metals washed out from the NMC are mainly located in areas covered by said thick film. Elevated amounts of NMC dissolution products are found in plated areas. Traces of nickel, manganese and cobalt are known to dissolve from the positive electrode and deposit on the graphite electrode, as the lithiated graphite quickly reduces most metal ions to their metallic form [50]. Such deposits are believed to strongly influence graphite aging and the formation of surface films, explaining the faster aging of graphite electrodes in actual batteries than in half cells consisting of graphite electrodes and lithium metal [41]. As reaction products of positive active material degradation are deposited on the negative electrode by reduction and as baseline contents are low, chemical analysis of the negative electrode is a good way to probe surface reactions of the positive electrode [7,8].

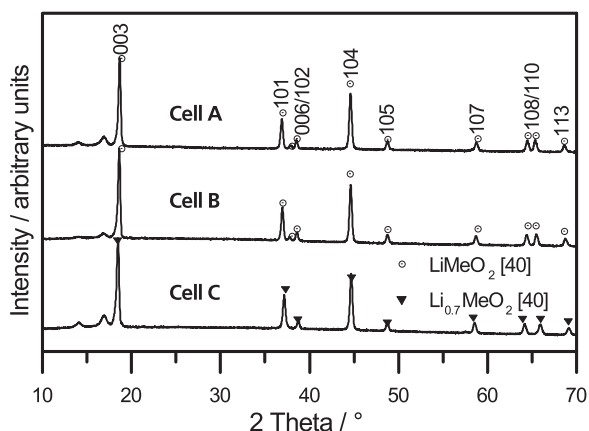


Fig. 3. NMC active material XRD patterns of samples taken from discharged cells A–C. Comparison to data from Choi et al. [40] shows that changes are due to a change in state of charge, not degradation.

### 3.1.4. Separator

The separator was inspected for clogging and degradation using scanning electron microscopy. Fig. 5(c) shows micrographs of both



**Table 3**  
Lattice parameters for  $R\bar{3}m$  phase obtained by Rietveld refinement of reference pattern [44], as well as lithiation  $x$  and lithium loss in  $\text{Li}_x\text{Ni}_{0.33}\text{Mn}_{0.33}\text{Co}_{0.33}\text{O}_2$  as deduced from Fig. 4. Given uncertainties are estimated by the standard deviations of the refinement and of the predictions based on calibration curves in Fig. 4.

Sample	Parameter $a/\text{nm}$ $a$	Lithiation $x$ deduced from $a$	Li-loss deduced from $a/\text{mAh}$ $\text{cm}^{-2}$	Parameter $c/\text{nm}$ $c$	Lithiation $x$ deduced from $c$	Li-loss deduced from $c/\text{mAh cm}^{-2}$
Cell A	$0.2853 \pm 0.0001$	$1.0 \pm 0.1$	0	$1.4242 \pm 0.0002$	$1.0 \pm 0.1$	0
Cell B	$0.2847 \pm 0.0002$	$0.9 \pm 0.1$	$0.44 \pm 0.04$	$1.4276 \pm 0.0002$	$0.9 \pm 0.1$	$0.33 \pm 0.02$
Cell C	$0.2832 \pm 0.0002$	$0.7 \pm 0.1$	$1.5 \pm 0.2$	$1.4387 \pm 0.0003$	$0.7 \pm 0.1$	$1.40 \pm 0.08$

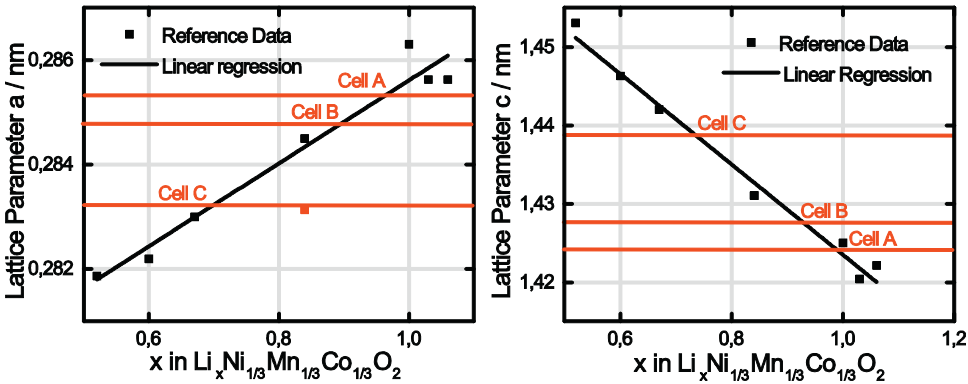


**Fig. 4.** Lattice parameters (a)  $a$  and (b)  $c$  are used to determine the lithiation of NMC. Published reference data [43,47,48] is used to calculate calibration lines  $a = [(0.0079 \pm 0.0008)x + (0.2777 \pm 0.0006)] \text{ nm}$  and  $c = [(0.058 \pm 0.003)x + (1.481 \pm 0.003)] \text{ nm}$ . One outlier from [47] was masked (red). (For interpretation of the references to color in this figure legend, the reader is referred to the web version of this article.)

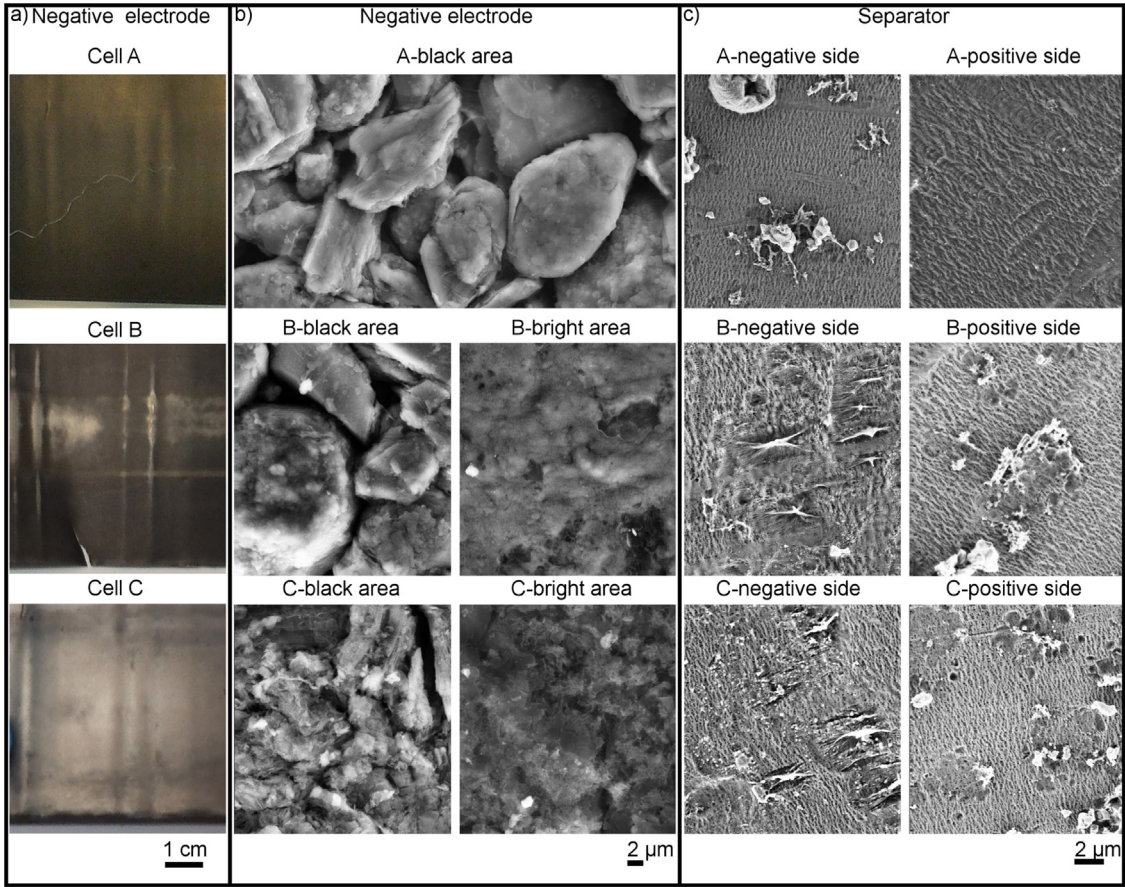


**Fig. 5.** (a) Plating on aged graphite electrodes: no plating is observed on pristine cell A. Cell B shows first plating as it has just started to degrade suddenly and cell C shows extended plating. (b) Scanning electron microscopy shows that black areas B-black area and C-black area resemble the pristine graphite of cell A, while B-bright area and C-bright area are degraded. (c) SEM micrographs of the separators of cells A–C. Areas of the negative facing side that came into contact with plated lithium show degradation.

**Table 4**

Lithium and Manganese contents detected on the negative electrodes of cells A–C using ICP-OES. Errors are based on measurement uncertainty of ICP-OES. Possible systematic errors caused by non-complete digestion add to uncertainty. Nonetheless, a clear trend in metal contents is observed.

Sample	Lithium content/ mAh cm <sup>-2</sup>	Manganese content/nmol cm <sup>-2</sup>
Cell A	0.25 ± 0.01	11 ± 1
Cell B	0.55 ± 0.01	33 ± 2
Cell C dark areas	0.85 ± 0.02	46 ± 2
C bright areas	1.87 ± 0.04	139 ± 7

sides of the separators taken from cells A–C. No changes are found on the side pointing to the positive electrode and in areas facing black parts of the negative electrode. The separators retain the original oriented porous structure with some minor imprints likely caused by compression. In contrast, where the separator was exposed to plated lithium, craters several micrometers in diameter can be observed in the micrographs. Those craters, visible on micrographs on the negative side of the separator taken from cells B and C, exhibit thick string-like aggregates. Their aspect points to localized melting or chemical degradation. This effect may have been caused by localized heating, mechanical causes or chemical interactions and shows the impact of lithium plating on the separator [14,51]. Plated lithium and the damaged separator influence the safety of lithium-ion cells in thermal and mechanical abuse scenarios [52].

### 3.2. Main degradation mechanism for lithium loss

Fig. 6 compares the capacity loss found during cycling to the lithium content found on the graphite electrode using chemical analysis by ICP-OES and to the lithium loss deduced by XRD measurements. Lithium found on the discharged electrode can be attributed to three main types. First, active lithium which is not extracted from the graphite upon discharge as voltage cutoff limits the potential of the negative electrode. Second, lithium compounds deposited on the graphite surface forming the so-called SEI. Third, lithium loss due to lithium plating, as described in literature [12,13,53–55]. Chemical analysis does not differentiate inactive lithium from buffered, potentially active lithium intercalated in the active graphite. Still the increasing lithium content of the negative electrode can be related to lithium loss, as the discharge potentials of the negative electrode increase over aging, which points to a loss of buffered lithium. Cell capacity and lithium loss found by XRD and ICP-OES show a similar trend upon aging. Additionally, analysis of the anode shows the importance of lithium plating. The lithium content found in samples of cells A and B as well as a sample from a dark area of cell C (C dark) show a trend similar to

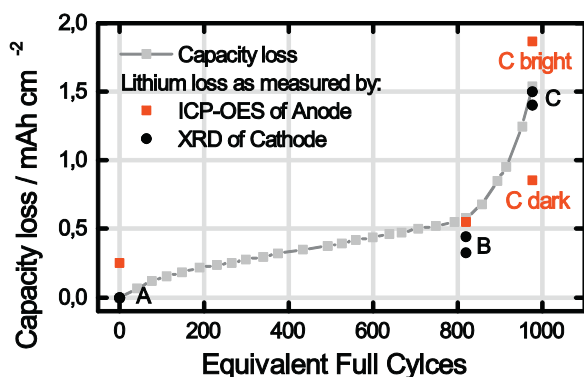


**Fig. 6.** Mean capacity loss of cycled 18650 cells compared to lithium content on the graphite electrode and delithiation of the cathode as found by XRD measurements.

the linear part of the capacity evolution. Lithium loss found in a sample taken from a bright area of cell C (C bright) explains the acceleration of the capacity loss. The inactive lithium found in this area is excessive. The deposition of inactive lithium species is the main aging mechanism observed and acceleration is caused by the defective areas.

#### 3.2.1. Evolution of electrochemical behavior

Fig. 7 In Fig. 7 the slow galvanostatic charge and discharge cycle (a) of the original cells, as well as the corresponding incremental capacity curves (b) are depicted. Cell A shows one major and three minor peaks, corresponding to the superimposition of the characteristic peaks of the graphite electrode and the broad curve of the NMC electrode. The characteristic peaks flatten out slowly during normal aging but vary rapidly as the battery changes its degradation behavior. Interestingly, the voltage region above 3.9 V appears nearly identical for all three aging states, with only a slight decrease in discharge voltage and incremental capacity. The peaks corresponding to the voltage plateaus in the range between 3.4 V and 3.9 V become smaller for cell B and partially disappear for cell C. A pronounced loss of incremental capacity in the range between 3.4 V and 3.9 V can be noticed. In the lower voltage region below 3.4 V no major changes are visible. It should be stressed that the charge and discharge profiles at the beginning of rapid degradation are only slightly changed compared to the pristine cell, making detection of this phenomenon very difficult without known history. Once the aging rate increases, the capacity in the lower voltage range drops heavily and the peaks almost disappear. A recent incremental analysis study on different commercial batteries reported very similar behavior, although a different positive active material was used [56,57].

To understand the exhibited phenomena, three-electrode laboratory cells from six locations on the unrolled jelly roll are constructed as described in Section 2. The laboratory cells are controlled by current and terminal voltage, while the reference electrode is used for monitoring of electrode potentials only. The same slow charge and discharge profiles as on original cells are applied. Based on the obtained potentials, incremental capacity analysis of the two electrodes' behavior is carried out. Samples are numbered based on the sampled cell and the specimen location by adding the number of the sampling spot as shown in Fig. 2 to the cells' abbreviation.

An overlay of incremental capacity curves obtained from pristine original and laboratory cells is shown in Fig. 10(a). Original and laboratory cells show similar behavior. Peak positions and capacity distribution as well as overall capacity compare well. The curves superimpose as expected from a homogeneous electrode. Results from laboratory cells are representative of the behavior in the commercial cells investigated.

Fig. 8 shows incremental capacity curves based on graphite and NMC electrode potential comparing B2 and B3 to pristine sample A5. With less than 25% capacity loss, sample B3 is representative of areas showing lesser extents of degradation, while sample B2 has lost more than 55% of its capacity. The NMC capacity curves do not change their shape but are cut off at lower lithium content upon aging. No signs for positive active material loss or changes in electrochemical behavior are visible in the samples. Capacity curves of the graphite electrode change in a more complicated manner. Sample B2 has suffered heavy degradation. Peak heights above 0.15 V are about one third smaller than in the pristine cell, a clear sign for pronounced active material loss. The peak at 0.10 V has vanished nearly completely. As this peak corresponds to highly lithiated states, this is a prominent sign for lithium loss, possibly due to nearby lithium plating. The loss of lithium content manifests in a shift to lower lithiation in the corresponding NMC electrode as is evident from the more positive cutoff potential. Sample

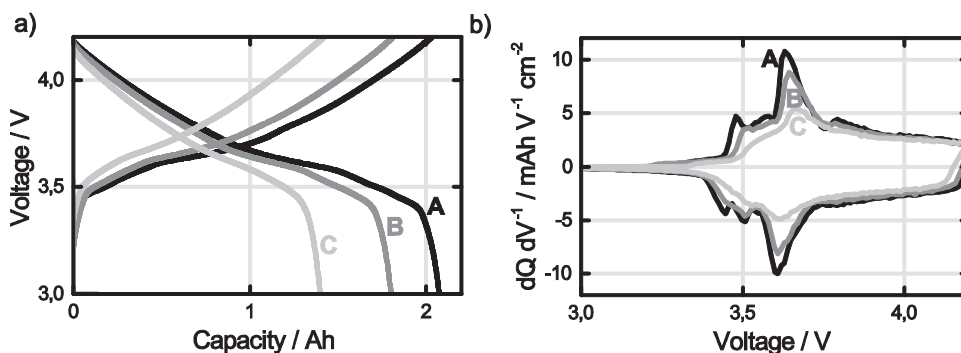


Fig. 7. (a) 0.02C full charge and discharge cycle performed before dissection of the original cells A–C. (b) Incremental capacity curves calculated from the same data.

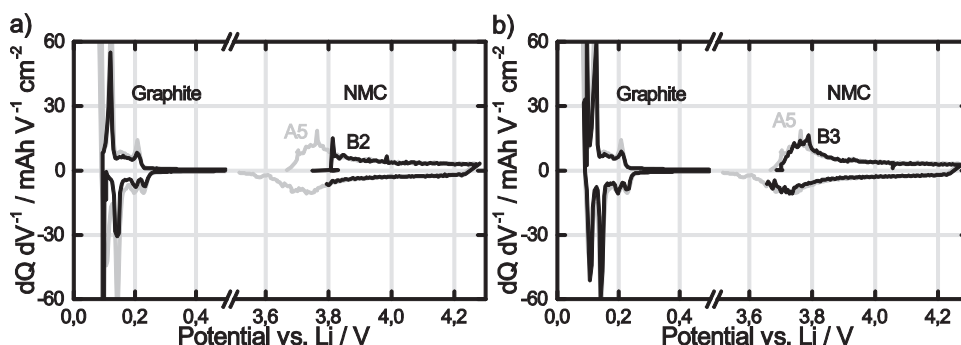


Fig. 8. Incremental capacities of samples B2 and B3 compared to sample A5 of the pristine cell. The incremental capacities of the more negative graphite and the more positive NMC are resolved for each sample.

B3 shows only slightly depressed peaks both for charging and discharging. Peak heights above 0.15 V are depressed by only about one eighth, indicating less active material loss. The peak at 0.10 V, corresponding to the high lithiation stage, is present. The conservation of this peak shows that lithium loss is slow in comparison to active material loss in areas that are not yet affected by rapid capacity loss. Therefore, it appears that slowly aging regions lose some active material and lithium, while areas degrading faster start to lose higher amounts of active graphite and excessive amounts of lithium.

The potential of graphite electrode discs sampled from the discharged cells and built into laboratory cells is compared in Fig. 9. The negative electrode discharges to higher potentials in more degraded areas. Samples with low capacity loss show unspecific behavior. Due to remaining lithium reserves and moderate discharge potentials, degradation of samples with low capacity loss is thought to be dominated by other factors. As the lithium

reserve is consumed and the final discharge potential of the graphite electrode is increased by lithium loss, a positive correlation seems to appear. Final discharge potential and capacity loss show a trend that can be explained by fast active material loss. There is some evidence in our previous studies and in literature that high depth of discharge may lead to increased material loss in graphite electrodes [3,37,58]. The volume changes associated with lithiation and delithiation are reported to cause contact loss by mechanical action and increased SEI formation [12,26,59]. Active material loss leads to lower potentials upon charging and therefore to higher lithium loss. Both the change in balancing and the increased overpotentials due to lower active surfaces and SEI formation may contribute to the more negative potentials during charging. Since less active graphite is available, remaining graphite does not only have to accommodate more lithium but also experiences higher current densities leading to higher overpotentials. Losses become more accentuated as the negative electrode reaches the potential of metallic lithium. The resulting irreversible lithium plating leads to further increased discharge potentials and a vicious circle ensues. Areas with initially less active graphite loss and lower current density are increasingly affected as lithium is consumed by defective areas thus also changing their final discharge potentials. Also, Oldham has shown that the edge of an electrochemically active area adjacent to an insulated area experiences excess currents [60]. The area experiencing plating rapidly expands and overall battery capacity drops. The resulting trend can be observed in Fig. 9 with some samples showing extreme capacity losses accompanied by high maximum potentials upon discharge.

### 3.2.2. Heterogeneous cell behavior

As pointed out in Section 3.2.1, some peaks in incremental capacity curves of aged cells start to disappear as degradation accelerates. In Fig. 10 incremental capacity curves of the sampled

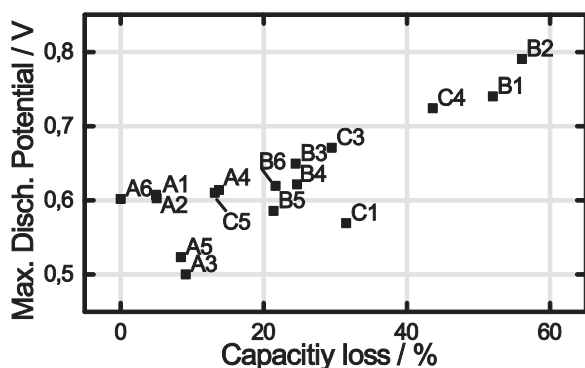


Fig. 9. Maximum potential of sampled graphite electrode discs as a function of capacity loss.



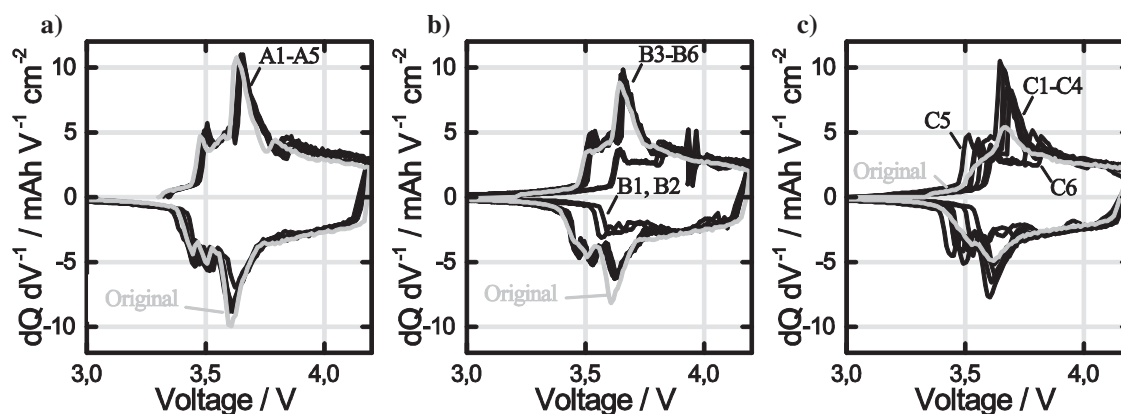


Fig. 10. Incremental capacity curves of sampled areas of cells (a) A, (b) B and (c) C are compared to original cells.

laboratory full cells are compared to the respective original cells. In Fig. 10(a), sample A6 is omitted due to excessive noise caused by a bad connection. In pristine cell A, all areas show uniform behavior with nearly no variation in peak position. Although aged, most areas of cell B show a comparable behavior. Samples collected from areas affected by lithium plating show different peak patterns with changed peak positions and greatly decreased capacities at lower voltages. Accordingly, the overall behavior below 3.9 V is slightly altered, too.

The effects on overall charge and discharge behavior of cell C are already very pronounced as a substantial portion of the battery has been affected by lithium plating. Sampled areas show marked differences in peak position and capacity in the lower voltage region. Highly altered profiles are found in five of six samples leading to peak smearing and a strong decay of capacity at lower voltages. For comparison, only two samples show altered capacity curves in cell B, but their aspect is already the same as found for many samples in cell C.

A simplified model of the cell is helpful to explain the changes in the original cell. Viewing the jelly roll as a parallel connection of degraded and nearly unaffected areas, its overall capacity is the sum over all areas. The overall incremental capacity per area is a function of several incremental capacity curves of areas in different stages of degradation. As increased aging begins, only a very small part of the surface exhibits changed behavior. Therefore, the impact on overall charge and discharge behavior is small, although local changes are dramatic. As rapid aging proceeds, more and larger parts of the electrode are affected. The impact of altered areas on the overall curve becomes more important due to their larger surface fraction. The broad variation of peak positions leads to a smeared overall behavior.

### 3.3. Identifying the cause for heterogeneous cell behavior

The initial onset of plating causes a sharp increase in aging rate. As this coincidence may explain the change in aging rate, we investigated the origin of the different patterns described in

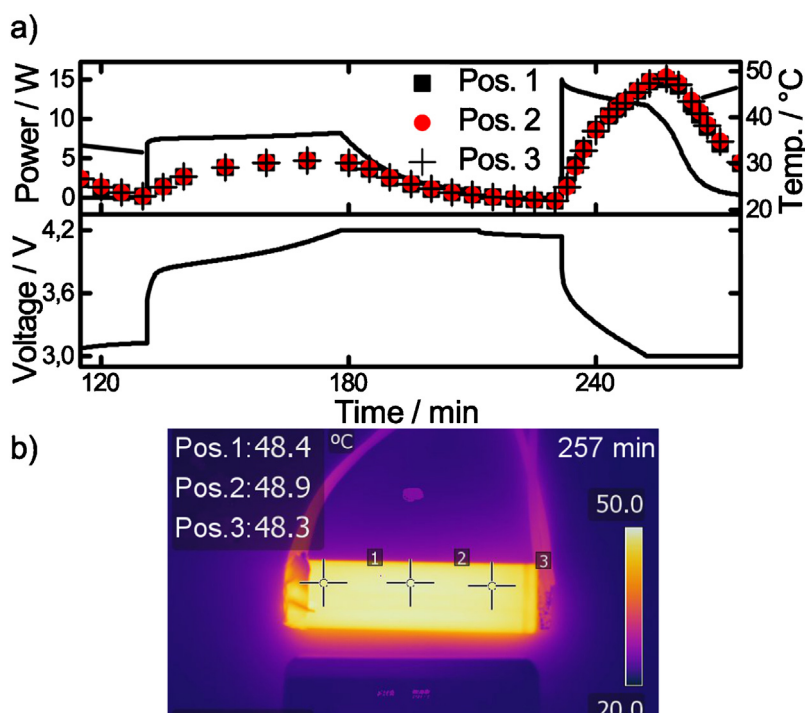


Fig. 11. Voltage, power and temperature evolution of an 18650 cell. Temperature of three surface points is logged using thermography. The thermograph shows the distribution at maximum temperature of the cell and position of the logged surface points.



paragraph 3.1.3 by thermography, computed tomography and post-mortem studies. A thin line is already present on pristine negative electrodes. This potential plating area is attributed to an unknown imperfection in the production process. Waldmann et al. recently showed that the pattern formed by axial stripes is caused by current collectors in cylindrical cells [33]. Lithium plating first appears in the central area of the electrode and on the edges of the regular axial stripes. For that reason it should be possible to identify the cause for plating by explaining the stripe pattern. Several reports on heterogeneous aging have been published recently and a number of possible explanations are given. The authors propose temperature, pressure and potential variations as possible causes of local plating [5,33,61–64]. However, potential variations caused by the resistance of the current collectors are not expected to cause patterns such as the regular axial stripes found in this study.

### 3.3.1. Temperature

Temperature gradients upon fast cycling of a pristine cell are investigated by thermal imaging. Fig. 11 shows the electrical power and voltage profiles during a full cycle together with the surface temperature measured on the three points shown in the thermograph below. The thermographic image shows the battery at peak temperature. The surface of the battery is heated up to more than 48 °C. Surface temperatures appear homogeneous. A small axial variation is visible; in contrast, no angular variation was detected. While radial gradients may have occurred [33,65], the stripe pattern found on the graphite electrodes is caused by angular variations. Such angular variations should be expected to be observable on the surface of the battery. Since no such variation is detected and due to the nature of the pattern, the pattern of axial stripes appears to have been caused by some other influence.

Besides the stripe pattern, plating also appears earlier in central areas than in the axially outer parts. The axial distribution of the surface temperature is investigated in order to discuss its possible influence on heterogeneous plating. To quantify the axial distribution, three measurement points are tracked over time. At the three points maximal temperatures of 48.4, 48.9 and 48.3 °C are found, respectively. The surface temperature varies by 0.6 °C

only. Compared to the overall temperature swing, the observed spatial temperature variation is small. Such a small variation is not expected to induce significant electrochemical differences. Nonetheless, already six cycles of the fast cycling protocol cause the stripes shown in Fig. 12(a) and (b). The observed temperature gradients do not seem to explain the double stripe pattern or axial variation of plating produced.

### 3.3.2. Compression

The computed tomographic image in Fig. 13 shows deformation of the jelly roll in a pristine cell. Fig. 12(a) and (b) shows plating patterns after fast, deep cycling. Plating occurs in comparable regions as in cells B and C and the regular stripe pattern already shown in cell B is reproduced. The current collector tab of the positive electrode marked as (1) in Fig. 13 creates a bulk close to the mandrel. The aluminum and separator foil surrounding the tab appear black in the tomographic image but cause further bulk. As the jelly roll is confined in the cylindrical stainless steel case, this bulk and the resulting deformation cause increased variations in compression. The bulk created by the negative current collector tab marked as (2) in Fig. 13 is less pronounced. Therefore, a minor effect is expected.

The stripe patterns shown in Fig. 12(b) can be clearly linked to the positive current collector tab (1) by their regular arrangement and occurrence in the inner part of the jelly roll [33]. As shown in Fig. 12(a), the negative current collector creates a much less pronounced effect, which is overlaid by the current gradient caused by the nearby positive current collector and the resistance of the copper foil.

The tabs are found to deform the jelly roll and therefore create spatial variations leading to plating especially near the edges of the imperfections. Heterogeneous pressure has been shown to have an effect on lithium ion diffusion through the separator [36,66] and to lead to localized defects in controlled experiments [67]. The effect of pressure may be attributed to changes in the separator's porosity and tortuosity [36,66,67]. In general, increased pressures are expected to show detrimental effects, even if slight compression

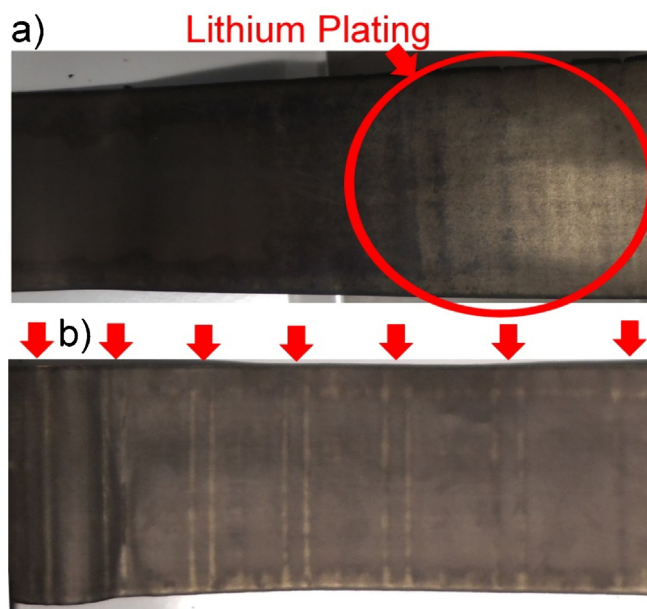


**Fig. 12.** (a) Outer part of the negative electrode exposed to 6 fast cycles. (b) Inner part of the same electrode showing a stripe pattern. Plating is marked by an ellipsis and arrows.

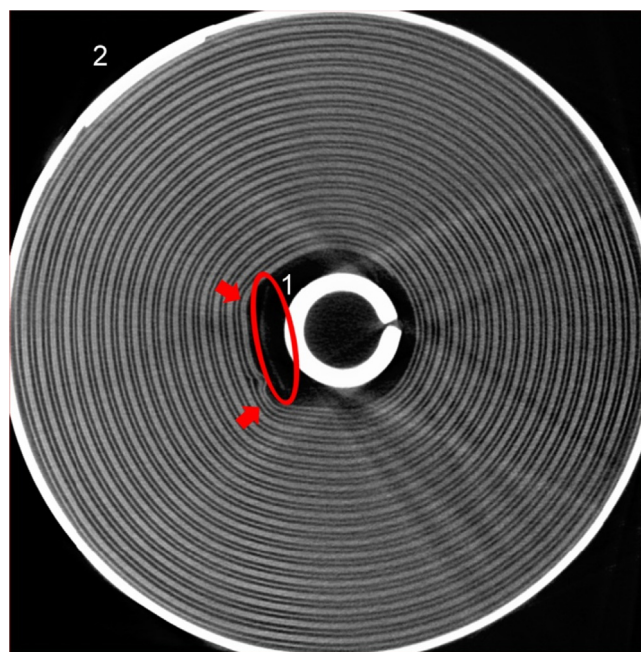


**Fig. 13.** (a) Computed tomographic crosscut of a pristine cell. The positive (1) and negative (2) current collector tabs are visible. The positive current collector is marked by an ellipsis, resulting deformations to the jelly rolls are marked by arrows. The positive current collector deforms the jelly roll.



**Fig. 14.** (a) A hose clamp is placed on a cell. (b) Plating is visible on the overlap of the current collector imprints and the clamp which are visualized by black and red rectangles respectively.

might be beneficial [36,66,68]. Additionally, the shape of an electrode has an influence on the diffusion regime in front of it. Oldham has shown that ridges may experience an excess current, while grooves experience reduced currents [69]. Variations in lithium concentration are known to contribute to overpotential [70,71].

As the battery ages and NMC potentials are shifted to higher potentials due to lithium loss, graphite maximum potentials rise, too. Deep discharge is reported to lead to active material loss in graphite electrodes [3,58]. Consequently, the capacity balancing of the two electrodes is gradually altered until the negative electrode becomes capacity limiting in some areas. Since the negative electrode operates very closely to lithium potential, plating may occur if the graphite capacity becomes inferior to locally available lithium in a given part.

#### 3.4. Control experiment for plating susceptibility

It is expected that large currents and voltage windows as well as low temperatures facilitate the occurrence of local plating. This localized plating is believed to cause subsequent rapid degradation. As a quick test, cells can be cycled at maximum permissible voltage swing and charge and discharge currents, exhausting the limits stated in the datasheet. Using constant voltage steps both upon charge and discharge of the cell, maximal states of charge can be obtained. Especially when soft packages are used, the cells should be tested in their final fixture. For a quick test for plating, cells are opened as soon as aging accelerates, or after a determined number of cycles. Using visual inspection, the negative electrodes are checked for plating.

Fig. 12(a) and (b) shows the outer and inner part of the graphite electrode of a cell subjected to such maximum strain cycling. The cell was cycled only 6 times and retains nearly 99% of its initial capacity. Already after 6 cycles plating has occurred. Patterns are found near the negative current collector tab and the positive current collector tab in the center of the cell. As can be seen in Fig. 12(a), the plated lithium near the negative current collector shows a slight stripe pattern but it is unclear if the plating is due to imprints from the negative current collector, or to the resistance gradient. A well-defined pattern of axial stripes is visible in Fig. 12(b), showing the inner part of the negative electrode. Plating occurs on the stripe pattern imprinted by the positive current collector, pointing to compression as the cause.

In a next step, a control experiment for the hypothesis on the influence of heterogeneous compression on plating is carried out. Local compression is applied by a clamp fixed around the diameter of cylindrical cells as shown in Fig. 14(a). The onset of lithium plating becomes even more localized and pronounced when we

apply a clamp on a pristine cell, as shown in Fig. 14(b). Patches of plated lithium appear on the overlap of the clamp and the current collector. These spots show highest compression and hence the strongest tendency to plating. This control experiment verifies the theory of compression induced plating and shows the detrimental effect of heterogeneous compression. The demonstrated induction of local plating by external compression qualitatively shows the influence of cell and pack design and mechanical constraints, as caused by unsuitable mounting and potting methods. Furthermore, this work shows how easily such defects can be detected by post-mortem inspection in sharp contrast to the complex detection using electric measurements on cell level which is often subject to interpretation.

#### 4. Conclusion

In this work, the causes for the sudden degradation of useable capacity have been studied by means of complementary methods such as computed tomography, post-mortem studies and electrochemical analyses. The results obtained point unanimously to heterogeneous aging as a key-factor for the sudden degradation of cell capacity, which in turn is triggered by differences in local compression.

At high states of health, the capacity fade rate is benign but some areas of the graphite electrode lose active material faster than others. Still, the localized changes are hardly noticeable on cell level due to averaging effects. First, lithium plating occurs in unevenly compressed areas, creating patterns visible to the human eye. Inactive lithium, thick passive films and increased deposition of manganese and other metals washed out from the positive active material are found in affected areas of cells B and C, opened at the onset of sudden degradation and 150 cycles later, respectively. As lithium plating leads to rapid consumption of active lithium, a sudden drop in capacity is observed on cell level. Lithium plating appears to spread out from the initial areas over the whole graphite electrode, quickly consuming the remaining useful lithium and active graphite. We hypothesize that a self-amplifying circle of reciprocal acceleration of local lithium loss and material loss causes rapid local degradation. Positive active material facing large patches of defective negative active material cannot be effectively utilized anymore. Incremental capacity analyses on cell level may mislead to the assumption of degradation on the positive electrode, even if only the negative electrode has deteriorated.

Using post-mortem analyses, a clear cause-effect chain linking compression differences to local lithium plating is established qualitatively. Further studies are necessary to quantify the effect of compression. It is hypothesized that avoiding the initial local

deposition of lithium metal can prevent the fatal kink in capacity retention. This can either be accomplished by more resistant negative active materials, robust cell design, or control measures avoiding critical states.

Battery cell designers can improve cycle life by homogeneous pressure distribution in the cell and using negative active materials that are resilient to elevated discharge potentials as they appear in aged cells such as improved carbons or lithium titanate. Also, a sufficiently oversized negative electrode and suitable electrolyte additives can help to avoid lithium plating [26,72]. When packs are designed, care must be taken not to exert local pressure on parts of cells and to avoid both very high and low states of charge. High currents are expected to be most critical in cells with designs causing inhomogeneities.

To benchmark different cell and pack designs regarding the risk of sudden rapid degradation, cells can be cycled at maximum permissible voltage swing and charge and discharge amperage followed by post-mortem analysis. While localized lithium plating in limited areas is hard to detect electrochemically, it can easily be detected by visual inspection. Based on our findings, the more cycles a battery can withstand this fast cycling regime without showing plating, the later it is expected to show rapid degradation. This test provides a relatively quick benchmark for an otherwise nearly unpredictable failure mode. The unfavorable performance of the cells investigated in this test explains why pronounced nonlinear behavior is found while other studies do not report such a behavior. Finally, the identified unfavorable control regimes allowing high currents in extreme states of charge are avoided in electromotive applications. It can be concluded that second life applications of automotive cells are not expected to be affected by compression-induced rapid deterioration.

## Acknowledgements

Funding from the German Federal Ministry for Economic Affairs and Energy (BMWi) as part of the EU-project ABattReLife and project management by the German Aerospace Center (DLR) are gratefully acknowledged. Furthermore, we thank Jan-Marcel Hausherr for carrying out the CT measurements at the Fraunhofer Center for High-Temperature Materials and Design. The responsibility for this publication rests with the authors.

## References

- [1] C.J. Rydh, B.A. Sandén, *Energ. Convers. Manage.* 46 (2005) 1980–2000, doi: <http://dx.doi.org/10.1016/j.enconman.2004.10.004>.
- [2] B. Scrosati, J. Garche, *J. Power Sour.* 195 (2010) 2419–2430, doi: <http://dx.doi.org/10.1016/j.jpowsour.2009.11.048>.
- [3] M. Ecker, N. Nieto, S. Käbitz, J. Schmalstieg, H. Blanke, A. Warnecke, D.U. Sauer, *J. Power Sour.* 248 (2014) 839–851, doi: <http://dx.doi.org/10.1016/j.jpowsour.2013.09.143>.
- [4] M. Broussely, P. Biensan, F. Bonhomme, P. Blanchard, S. Herreyre, K. Nechev, R. Staniewicz, *J. Power Sour.* 146 (2005) 90–96, doi: <http://dx.doi.org/10.1016/j.jpowsour.2005.03.172>.
- [5] E. Sarasketa-Zabala, F. Aguesse, I. Villarreal, L.M. Rodriguez-Martinez, C.M. López, P. Kubiak, *J. Phys. Chem. C* 119 (2015) 896–906, doi: <http://dx.doi.org/10.1021/jp510071d>.
- [6] X. Feng, J. Sun, M. Ouyang, X. He, L. Lu, X. Han, M. Fang, H. Peng, *J. Power Sour.* 272 (2014) 457–467, doi: <http://dx.doi.org/10.1016/j.jpowsour.2014.08.094>.
- [7] B. Stiaszny, J.C. Ziegler, E.E. Krauß, J.P. Schmidt, E. Ivers-Tiffée, *J. Power Sour.* 251 (2014) 439–450, doi: <http://dx.doi.org/10.1016/j.jpowsour.2013.11.080>.
- [8] B. Stiaszny, J.C. Ziegler, E.E. Krauß, M. Zhang, J.P. Schmidt, E. Ivers-Tiffée, *J. Power Sour.* 258 (2014) 61–75, doi: <http://dx.doi.org/10.1016/j.jpowsour.2014.02.019>.
- [9] X. Han, M. Ouyang, L. Lu, J. Li, Y. Zheng, Z. Li, *J. Power Sour.* (2013), doi: <http://dx.doi.org/10.1016/j.jpowsour.2013.11.029>.
- [10] M. Broussely, S. Herreyre, P. Biensan, P. Kaszlejna, K. Nechev, R. Staniewicz, *J. Power Sour.* 97–98 (2001) 13–21, doi: [http://dx.doi.org/10.1016/S0378-7753\(01\)00722-4](http://dx.doi.org/10.1016/S0378-7753(01)00722-4).
- [11] Y. Li, M. Bettge, B. Polzin, Y. Zhu, M. Balasubramanian, D.P. Abraham, *J. Electrochem. Soc.* 160 (2013) A3006, doi: <http://dx.doi.org/10.1149/2.002305jes>.
- [12] J. Vetter, P. Novák, M. Wagner, C. Veit, K.-C. Möller, J. Besenhard, M. Winter, M. Wohlfahrt-Mehrens, C. Vogler, A. Hammouch, *J. Power Sour.* 147 (2005) 269–281, doi: <http://dx.doi.org/10.1016/j.jpowsour.2005.01.006>.
- [13] A. Barré, B. Deguilhem, S. Grolleau, M. Gérard, F. Suard, D. Riu, *J. Power Sour.* 241 (2013) 680–689, doi: <http://dx.doi.org/10.1016/j.jpowsour.2013.05.040>.
- [14] V. Agubra, J. Fergus, *Materials* 6 (2013) 1310–1325, doi: <http://dx.doi.org/10.3390/ma6041310>.
- [15] M. Grützke, V. Kraft, B. Hoffmann, S. Klamor, J. Diekmann, A. Kwade, M. Winter, S. Nowak, *J. Power Sour.* 273 (2015) 83–88, doi: <http://dx.doi.org/10.1016/j.jpowsour.2014.09.064>.
- [16] G. Gachot, S. Grugeon, M. Armand, S. Pilard, P. Guenot, J.-M. Tarascon, S. Laruelle, *J. Power Sour.* 178 (2008) 409–421, doi: <http://dx.doi.org/10.1016/j.jpowsour.2007.11.110>.
- [17] P. Handel, G. Fauler, K. Kapper, M. Schmuck, C. Stangl, R. Fischer, F. Uhlig, S. Koller, *J. Power Sour.* 267 (2014) 255–259, doi: <http://dx.doi.org/10.1016/j.jpowsour.2014.05.080>.
- [18] V. Kraft, W. Weber, M. Grützke, M. Winter, S. Nowak, *RSC Adv.* 5 (2015) 80150–80157, doi: <http://dx.doi.org/10.1039/C5RA16679A>.
- [19] V. Kraft, M. Grützke, W. Weber, M. Winter, S. Nowak, *J. Chromatogr. A* 1354 (2014) 92–100, doi: <http://dx.doi.org/10.1016/j.chroma.2014.05.066>.
- [20] D.Y. Wang, N. Sinha, R. Petibon, J. Burns, J.R. Dahn, *J. Power Sour.* 251 (2014) 311–318, doi: <http://dx.doi.org/10.1016/j.jpowsour.2013.11.064>.
- [21] S.S. Zhang, *J. Power Sour.* 162 (2006) 1379–1394, doi: <http://dx.doi.org/10.1016/j.jpowsour.2006.07.074>.
- [22] H.J. Ploehn, P. Ramadass, R.E. White, *J. Electrochem. Soc.* 151 (2004) A456, doi: <http://dx.doi.org/10.1149/1.1644601>.
- [23] M. Ecker, J.B. Gerschler, J. Vogel, S. Käbitz, F. Hust, P. Dechent, D.U. Sauer, *J. Power Sour.* 215 (2012) 248–257, doi: <http://dx.doi.org/10.1016/j.jpowsour.2012.05.012>.
- [24] J. Wang, J. Purewal, P. Liu, J. Hicks-Garner, S. Soukiazian, E. Sherman, A. Sorenson, L. Vu, H. Tataria, M.W. Verbrugge, *J. Power Sour.* 269 (2014) 937–948, doi: <http://dx.doi.org/10.1016/j.jpowsour.2014.07.030>.
- [25] J. Schmalstieg, S. Käbitz, M. Ecker, D.U. Sauer, *J. Power Sour.* 257 (2014) 325–334, doi: <http://dx.doi.org/10.1016/j.jpowsour.2014.02.012>.
- [26] J.C. Burns, A. Kassam, N.N. Sinha, L.E. Downie, L. Solnickova, B.M. Way, J.R. Dahn, *J. Electrochem. Soc.* 160 (2013) A1451, doi: <http://dx.doi.org/10.1149/2.060309jes>.
- [27] M. Petzl, M.A. Danzer, *J. Power Sour.* 254 (2014) 80–87, doi: <http://dx.doi.org/10.1016/j.jpowsour.2013.12.060>.
- [28] Z. Li, J. Huang, B. Yann Liaw, V. Metzler, J. Zhang, *J. Power Sour.* 254 (2014) 168–182, doi: <http://dx.doi.org/10.1016/j.jpowsour.2013.12.099>.
- [29] J.-i. Yamaki, S.-i. Tobishima, K. Hayashi, Keiichi Saito, Y. Nemoto, M. Arakawa, *J. Power Sour.* 74 (1998) 219–227, doi: [http://dx.doi.org/10.1016/S0378-7753\(98\)00067-6](http://dx.doi.org/10.1016/S0378-7753(98)00067-6).
- [30] E. Peled, *J. Electrochem. Soc.* 126 (1979 2047), doi: <http://dx.doi.org/10.1149/1.2128859>.
- [31] K. Jalkanen, J. Karppinen, L. Skogström, T. Laurila, M. Nisula, K. Vuorilehto, *Appl. Energy* 154 (2015) 160–172, doi: <http://dx.doi.org/10.1016/j.apenergy.2015.04.110>.
- [32] F. Sagane, R. Shimokawa, H. Sano, H. Sakaeb, Y. Iriyama, *J. Power Sour.* 225 (2013) 245–250, doi: <http://dx.doi.org/10.1016/j.jpowsour.2012.10.026>.
- [33] T. Waldmann, S. Gorse, T. Samtleben, G. Schneider, V. Knoblauch, M. Wohlfahrt-Mehrens, *J. Electrochem. Soc.* 161 (2014) A1742, doi: <http://dx.doi.org/10.1149/2.1001410jes>.
- [34] M. Dubarry, C. Truchot, B.Y. Liaw, K. Gering, S. Sazhin, D. Jamison, C. Michelbacher, *J. Electrochem. Soc.* 160 (2012) A191, doi: <http://dx.doi.org/10.1149/2.063301jes>.
- [35] M. Zier, F. Scheiba, S. Oswald, J. Thomas, D. Goers, T. Scherer, M. Klose, H. Ehrenberg, J. Eckert, *J. Power Sour.* 266 (2014) 198–207, doi: <http://dx.doi.org/10.1016/j.jpowsour.2014.04.134>.
- [36] J. Cannarella, C.B. Arnold, *J. Electrochem. Soc.* 162 (2015) A1365, doi: <http://dx.doi.org/10.1149/2.1051507jes>.
- [37] S.F. Schuster, T. Bach, E. Fleder, J. Müller, M. Brand, G. SEXTL, A. Jossen, *J. Energy Storage* 1 (2015) 44–53, doi: <http://dx.doi.org/10.1016/j.jest.2015.05.003>.
- [38] X. Feng, J. Li, M. Ouyang, L. Lu, J. Li, X. He, *J. Power Sources* 232 (2013) 209–218, doi: <http://dx.doi.org/10.1016/j.jpowsour.2013.01.018>.
- [39] J.P. Christophersen, S.R. Shaw, *J. Power Sour.* 195 (2010) 1225–1234, doi: <http://dx.doi.org/10.1016/j.jpowsour.2009.08.094>.
- [40] J. Choi, A. Manthiram, *J. Electrochem. Soc.* 152 (2005) A1714, doi: <http://dx.doi.org/10.1149/1.1954927>.
- [41] H. Zheng, Q. Sun, G. Liu, X. Song, V.S. Battaglia, *J. Power Sour.* 207 (2012) 134–140, doi: <http://dx.doi.org/10.1016/j.jpowsour.2012.01.122>.
- [42] F. Rosciano, J.-F. Colin, F. La Mantia, N. Tran, P. Novák, *Electrochem. Solid-State Lett.* 12 (2009) A140, doi: <http://dx.doi.org/10.1149/1.3130042>.
- [43] N. Yabuuchi, Y. Makimura, T. Ohzuku, *J. Electrochem. Soc.* 154 (2007) A314, doi: <http://dx.doi.org/10.1149/1.2455585>.
- [44] Y. Idemoto, T. Matsui, *Electrochemistry* 75 (2007) 791–799, doi: <http://dx.doi.org/10.5796/electrochemistry.75.791>.
- [45] O. Dolotko, A. Senyshyn, M.J. Mühlbauer, K. Nikolowski, H. Ehrenberg, *J. Power Sour.* 255 (2014) 197–203, doi: <http://dx.doi.org/10.1016/j.jpowsour.2014.01.010>.
- [46] X.-L. Wang, K. An, L. Cai, Z. Feng, S.E. Nagler, C. Daniel, K.J. Rhodes, A.D. Stoica, H.D. Skorpenske, C. Liang, W. Zhang, J. Kim, Y. Qi, S.J. Harris, *Sci. Rep.* 2 (2012) 747, doi: <http://dx.doi.org/10.1038/srep00747>.
- [47] S.-C. Yin, Y.-H. Rho, I. Swainson, L.F. Nazar, *Chem. Mater.* 18 (2006) 1901–1910, doi: <http://dx.doi.org/10.1021/cm0511769>.



- [48] N.-S. Choi, Z. Chen, S.A. Freunberger, X. Ji, Y.-K. Sun, K. Amine, G. Yushin, L.F. Nazar, J. Cho, P.G. Bruce, *Angew. Chem. Int. Ed.* 51 (2012) 9994–10024, doi: <http://dx.doi.org/10.1002/anie.201201429>.
- [49] M. Wohlfahrt-Mehrens, C. Vogler, J. Garche, *J. Power Sour.* 127 (2004) 58–64, doi: <http://dx.doi.org/10.1016/j.jpowsour.2003.09.034>.
- [50] F. Lin, I.M. Markus, D. Nordlund, T.-C. Weng, M.D. Asta, H.L. Xin, M.M. Doeff, *Nat. Commun.* 5 (2014), doi: <http://dx.doi.org/10.1038/ncomms4529>.
- [51] M. Dollé, L. Sannier, B. Beaudoin, M. Trentin, J.-M. Tarascon, *Electrochem. Solid-State Lett.* 5 (2002) A286, doi: <http://dx.doi.org/10.1149/1.1519970>.
- [52] M. Fleischhammer, T. Waldmann, G. Bisle, B.-I. Hogg, M. Wohlfahrt-Mehrens, *J. Power Sour.* 274 (2015) 432–439, doi: <http://dx.doi.org/10.1016/j.jpowsour.2014.08.135>.
- [53] M. Dubarry, C. Truchot, B.Y. Liaw, *J. Power Sour.* 219 (2012) 204–216, doi: <http://dx.doi.org/10.1016/j.jpowsour.2012.07.016>.
- [54] A. Barré, F. Suard, M. Gérard, M. Montaru, D. Riu, *J. Power Sour.* 245 (2014) 846–856, doi: <http://dx.doi.org/10.1016/j.jpowsour.2013.07.052>.
- [55] M. Ouyang, Z. Chu, L. Lu, J. Li, X. Han, X. Feng, G. Liu, *J. Power Sour.* 286 (2015) 309–320, doi: <http://dx.doi.org/10.1016/j.jpowsour.2015.03.178>.
- [56] M. Dubarry, C. Truchot, B.Y. Liaw, K. Gering, S. Sazhin, D. Jamison, C. Michelbacher, *J. Power Sour.* 196 (2011) 10336–10343, doi: <http://dx.doi.org/10.1016/j.jpowsour.2011.08.078>.
- [57] M. Dubarry, C. Truchot, M. Cugnet, B.Y. Liaw, K. Gering, S. Sazhin, D. Jamison, C. Michelbacher, *J. Power Sour.* 196 (2011) 10328–10335, doi: <http://dx.doi.org/10.1016/j.jpowsour.2011.08.077>.
- [58] V.A. Sethuraman, L.J. Hardwick, V. Srinivasan, R. Kostecki, *J. Power Sour.* 195 (2010) 3655–3660, doi: <http://dx.doi.org/10.1016/j.jpowsour.2009.12.034>.
- [59] D. Aurbach, *Solid State Ionics* 148 (2002) 405–416, doi: [http://dx.doi.org/10.1016/S0167-2738\(02\)00080-2](http://dx.doi.org/10.1016/S0167-2738(02)00080-2).
- [60] K.B. Oldham, *J. Electroanal. Chem. Interfacial Electrochem.* 122 (1981) 1–17, doi: [http://dx.doi.org/10.1016/S0022-0728\(81\)80136-2](http://dx.doi.org/10.1016/S0022-0728(81)80136-2).
- [61] M. Klett, R. Eriksson, J. Groot, P. Svens, K. Ciosek Högstöm, R.W. Lindström, H. Berg, T. Gustafson, G. Lindbergh, K. Edström, *J. Power Sour.* 257 (2014) 126–137, doi: <http://dx.doi.org/10.1016/j.jpowsour.2014.01.105>.
- [62] N. Zhang, H. Tang, *J. Power Sour.* 218 (2012) 52–55, doi: <http://dx.doi.org/10.1016/j.jpowsour.2012.06.071>.
- [63] W. Zhao, G. Luo, C.-Y. Wang, *J. Power Sour.* 257 (2014) 70–79, doi: <http://dx.doi.org/10.1016/j.jpowsour.2013.12.146>.
- [64] L. Cai, K. An, Z. Feng, C. Liang, S.J. Harris, *J. Power Sources* 236 (2013) 163–168, doi: <http://dx.doi.org/10.1016/j.jpowsour.2013.02.066>.
- [65] T. Waldmann, M. Wohlfahrt-Mehrens, *ECS Electrochem. Lett.* 4 (2014) A1, doi: <http://dx.doi.org/10.1149/2.0031501eel>.
- [66] J. Cannarella, C.B. Arnold, *J. Power Sour.* 226 (2013) 149–155, doi: <http://dx.doi.org/10.1016/j.jpowsour.2012.10.093>.
- [67] J. Cannarella, C.B. Arnold, *J. Power Sour.* 245 (2014) 745–751, doi: <http://dx.doi.org/10.1016/j.jpowsour.2013.06.165>.
- [68] A. Barai, Y. Guo, A. McGordon, P. Jennings (Eds.) A study of the effects of external pressure on the electrical performance of a lithium-ion pouch cell, *IEEE*, 10.1109/ICCVE.2013.6799809.
- [69] K.B. Oldham, *J. Solid State Electrochem.* 1 (1997) 36–44, doi: <http://dx.doi.org/10.1007/s100080050020>.
- [70] R. Chandrasekaran, *J. Power Sour.* 262 (2014) 501–513, doi: <http://dx.doi.org/10.1016/j.jpowsour.2014.03.124>.
- [71] B.K. Purushothaman, U. Landau, *J. Electrochem. Soc.* 153 (2006) A533, doi: <http://dx.doi.org/10.1149/1.2161580>.
- [72] C.-S. Kim, K.M. Jeong, K. Kim, C.-W. Yi, *Electrochim. Acta* 155 (2015) 431–436, doi: <http://dx.doi.org/10.1016/j.electacta.2014.12.005>.